Pixel space convolution for cosmic microwave background experiments

P. Fluxá,[a] **M.K. Brewer,**[b] **R. Dünner**[a]

[a]Instituto de Astrofísica, Pontificia Universidad Católica de Chile ,
  Vicuña Mackenna 4860, Chile
[b]Department of Astronomy, Johns Hopkins University,
  Baltimore MD, USA

  E-mail: pafluxa@astro.puc.cl, brewer@astro.umass.edu, rdunner@astro.puc.cl

Abstract.   Cosmic microwave background experiments have experienced an exponential increase in complexity, data size and sensitivity. One of the goals of current and future experiments is to characterize the B-mode power spectrum, which would be considered a strong evidence supporting inflation. The signal associated with inflationary B-modes is very weak, and so a successful detection requires exquisite control over systematic effects, several of which might arise due to the interaction between the electromagnetic properties of the telescope beam, the scanning strategy and the sky model. In this work, we present the Pixel Space COnvolver (PISCO), a new software tool capable of producing mock data streams for a general CMB experiment. PISCO uses a fully polarized representation of the electromagnetic properties of the telescope. PISCO also exploits the massively parallel architecture of Graphic Processing Units to speed-up the main calculation. This work shows the results of applying PISCO in several scenarios, included a realistic simulation of an ongoing experiment, the Cosmology Large Angular Scale Surveyor.

Contents

1 Introduction

The study of the cosmic microwave background (CMB) in the last few decades has lead to major advances in Cosmology. In particular, the study of the temperature and polarization anisotropy field has allowed us to achieve percent level constraints on cosmological parameters, favoring a universe dominated by cold dark matter plus a cosmological constant (ΛCDM), known today as the standard model of Cosmology (see [21]). Current efforts are mostly focused on the polarization anisotropy field, as it promises to provide independent constraints on the very early stages of the Universe. At these very first moments, the leading theory predicts that the Universe exponentially expanded nearly 60 e-folds in a process called inflation, becoming the flat, homogeneous and isotropic Universe that we see today. If true, gravitational waves generated by this expansion would have later interacted with the surface of last scatter, leaving a unique imprint in the polarization field which should be observable today.

Electromagnetic radiation from the CMB anisotropy field is nearly 10% polarized. These polarized anisotropies can be modeled as a spin-2 field, which is separable in two orthogonal components: a curl-free component called E-mode, and a divergence-free component called B-mode. In the absence of gravitational waves, the polarization field would contain only E-modes, which would be partially turned into B-modes by gravitational lensing. The resulting B-mode field would be one or more orders of magnitude lower than the E-mode signal, being very faint and difficult to measure. Moreover, recent results show that this signal lies below other polarized emissions, like the interstellar medium (see [4]), indicating that detection of the primordial B-mode signal is indeed a major technical challenge.

Another source of confusion is experimental systematic effects. The tremendous increase in sensitivity of CMB experiments has brought into play a long list of instrumental and observational effects, which need to be properly incorporated not only into the data reduction process, but into the design of future experiments as well. Because the CMB is an extended signal on the sky, it is crucial to characterize the beam, or in the more general case, the polarized antenna response of the telescope. It is also key to model and understand how this response gets convolved with the sky signal via the given scanning strategy, as this process may directly affect the scientific results.

Modeling the effect of the telescope beam on scientific results can be done analytically or numerically. For instance, the effect of symmetrical beams with smooth profiles can be analytically accounted for when computing the power spectra of CMB maps (see [19]). The impact of other related systematic effects, like beam mismatch, has also been described in the literature (see [7, 18, 25]). When the beam has more complex features, like sidelobes, numerical methods must be used instead. Several techniques that rely on harmonic space representations of the beam (see [1]) the sky and the scanning strategy have been devised (see [5, 26]). An excellent description of an implementation of this is given in [8]. Another approach is the one followed by FeBeCop (see [17]), which computes an effective beam instead of convolving the sky for every time sample.

In this work, we describe the algorithm and prototype implementation of a new CMB computer simulation code, the Pixel Space COnvolver (PISCO). PISCO has the capability of accounting for arbitrary shaped, time-varying beams and sky models. Polarization properties of the beam are handled following the work presented in [18]. PISCO also exploits the massively parallel architecture that Graphics Processing Units (GPU) provide via the CUDA application programming interface, and was designed from scratch to take advantage of HPC environments.

This paper is organized as follows. §2 contains a description of the coordinate system and geometrical transformations used to model an antenna pointing at the sky. §3 and §4 describe the methodology that was used to model the polarizing properties of an antenna and its coupling to the sky. §5 describes the algorithm used by PISCO, as well as a prototype implementation. §6 presents validation tests on the prototype implementation of PISCO. §7 provides an example
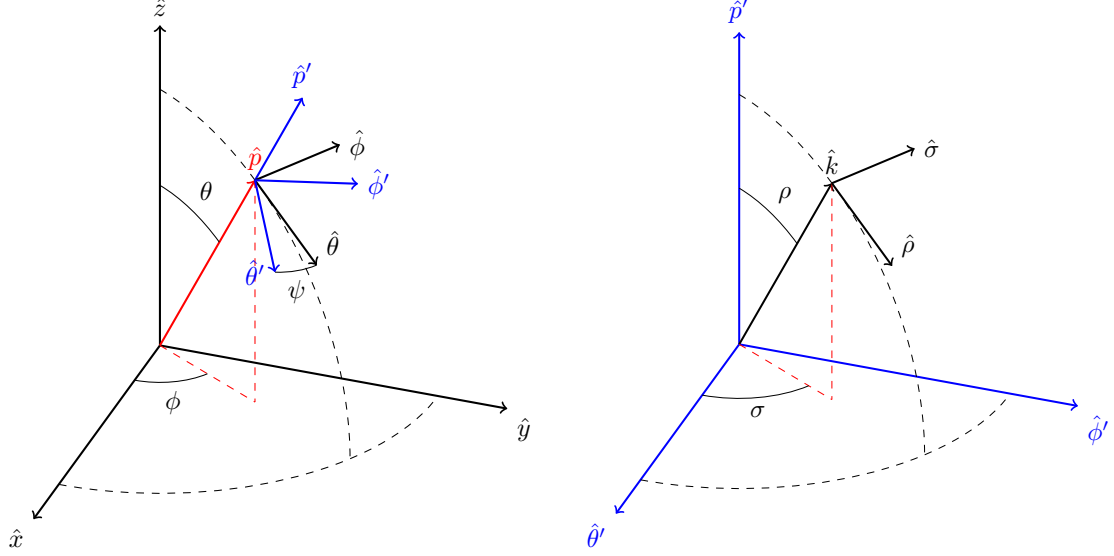
Figure 1. Left panel: sky basis. The sky basis is a generic spherical coordinate system. $\hat{x}$, $\hat{y}$ and $\hat{z}$ form an orthonormal basis. Unit vector $\hat{p}$ is defined by its spherical coordinates, co-latitude θ and longitude ϕ. Co-latitude increases from the north pole towards the south pole. Longitude increases from west to east. Tangent vectors at $\hat{p}$, $\hat{\theta}$ and $\hat{\phi}$, can be rotated around $\hat{p}$ by angle ψ to generate vectors $\hat{\theta}'$ and $\hat{\phi}'$. Note an observer looking towards the sky along $\hat{p}$ will measure angle ψ as increasing clockwise from South. Right panel: the antenna basis is built using spherical unit vectors $\hat{\theta}'$, $\hat{\phi}'$ and $\hat{p}'$, analogous to Cartesian unit vectors $\hat{x}$, $\hat{y}$ and $\hat{z}$. The orientation of the antenna basis with respect to the sky basis is completely determined by the pointing vector $\hat{p}$ and rotation angle ψ. A unit vector $\hat{k}$ in the antenna basis is described by ρ (co-latitude) and σ (longitude). Tangent vectors at $\hat{k}$ are $\hat{\rho}$ and $\hat{\sigma}$.

application of PISCO to the Cosmology Large Angular Scale Surveyor, CLASS ([12]). The paper concludes with a brief discussion of the results obtained in §8.

2   Coordinates

Since PISCO performs the convolution of the polarized antenna response with the sky in the spatial domain, it makes extensive use of coordinate transformations. These operations can be described by the use of two complementary spherical coordinate systems, which are described in Figure 1. The first coordinate system corresponds to the *sky basis*. Unit base vectors of these coordinate system are $\hat{x}$, $\hat{y}$ and $\hat{z}$. For convenience, the antenna pointing in the sky basis will be described as a 3-tuple $\bar{q}$, so that an antenna aiming at co-latitude θ_0 and longitude ϕ_0, with position angle ψ_0 has a pointing

$$\bar{q}_0 = (\theta_0, \phi_0, \psi_0)\,. \tag{2.1}$$

Then the *pointing direction*, denoted by vector $\hat{p}_0$, can be expressed as a linear combination of base vectors and spherical coordinates (θ_0, ϕ_0) via

$$\hat{p}_0 = \sin(\theta_0)\cos(\phi_0)\hat{x} + \sin(\theta_0)\sin(\phi_0)\hat{y} + \cos(\theta_0)\hat{z}\,. \tag{2.2}$$

The vectors $\hat{\theta}_0$ and $\hat{\phi}_0$ are computed using

$$\begin{aligned}
\hat{\theta}_0 =&\ \cos(\theta_0)\cos(\phi_0)\hat{x} + \cos(\theta_0)\sin(\phi_0)\hat{y} - \sin(\theta_0)\hat{z} \\
\hat{\phi}_0 =&\ \qquad\qquad\qquad -\sin(\phi_0)\hat{x} + \cos(\phi_0)\hat{y}\,.
\end{aligned} \tag{2.3}$$

These vectors can be used to build a second coordinate system, the *antenna basis*. Given an antenna pointing $\bar{q}_0$, the antenna basis base vectors can be written in terms of sky basis coordinates as

$$\hat{p}_0' = \hat{p}_0 \tag{2.4}$$

$$\hat{\theta}_0' = \cos(\psi_0)\hat{\theta}_0 + \sin(\psi_0)\hat{\phi}_0 \tag{2.5}$$

$$\hat{\phi}_0' = -\sin(\psi_0)\hat{\theta}_0 + \cos(\psi_0)\hat{\phi}_0 \,. \tag{2.6}$$

In the antenna basis, coordinates analog to sky basis co-latitude and longitude are ρ and σ, respectively. As in equation 2.2, a vector $\hat{k}$ can be similarly written in terms of antenna basis coordinates as

$$\hat{k} = \sin(\rho)\cos(\sigma)\hat{\theta}_0' + \sin(\rho)\sin(\sigma)\hat{\phi}_0' + \cos(\rho)\hat{p}_0' \tag{2.7}$$

while vectors analog to the ones described by equation 2.3 are

$$\begin{aligned} \hat{\rho} &= \cos(\rho)\cos(\sigma)\hat{\theta}_0' + \sin(\rho)\sin(\sigma)\hat{\phi}_0' - \sin(\rho)\hat{p}_0' \\ \hat{\sigma} &= -\sin(\sigma)\hat{\theta}_0' + \cos(\sigma)\hat{\phi}_0' \,. \end{aligned} \tag{2.8}$$

In many situations, antennas are equipped with polarization sensitive devices. The direction on the sky for which the device has maximum sensitivity to linearly polarized radiation is called co-polarization, denoted by $\hat{e}_\parallel$. The perpendicular direction, known as cross-polarization, is denoted by $\hat{e}_\times$. Because polarization is defined in the sky basis (see Figure 2), a polarization sensitive antenna must compensate for the apparent rotation of its own polarization basis with respect to the sky. This can be accomplished by rotating the incoming Stokes vector by the angle between $\hat{e}_\parallel$ and $\hat{\theta}$, namely

$$\chi(\rho, \sigma) = \arctan\left(\frac{|\hat{e}_\parallel \times \hat{\theta}|}{\hat{e}_\parallel \cdot \hat{\theta}}\right) \,. \tag{2.9}$$

See Appendix A for details on the definition of co-polarization and cross-polarization that PISCO uses and the computation of $\chi(\rho, \sigma)$ using spherical trigonometry.

3   A polarized model for antennas

The properties of an antenna equipped with detectors that are insensitive to polarization can be fully characterized by its beam. The beam is defined in terms of the antenna angular power density distribution $U(\rho, \sigma)$ via

$$b(\rho, \sigma) = \frac{U(\rho, \sigma)}{\max[U(\rho, \sigma)]} = \frac{U(\rho, \sigma)}{U(0,0)} \,. \tag{3.1}$$

From this definition of the beam, a standard quantification of an antenna's ability to direct power to a particular region of the sky is given by the beam solid angle Ω, calculated as

$$\Omega = \int_{4\pi} b(\rho, \sigma) \, \mathrm{d}\Omega \,. \tag{3.2}$$

These concepts fully characterize a lossless antenna in the case it is not sensitive to polarization, while modern CMB experiments, aim at measuring E-modes and B-modes. It then becomes necessary to introduce a more general treatment of the antenna, so as to include its polarizing properties.
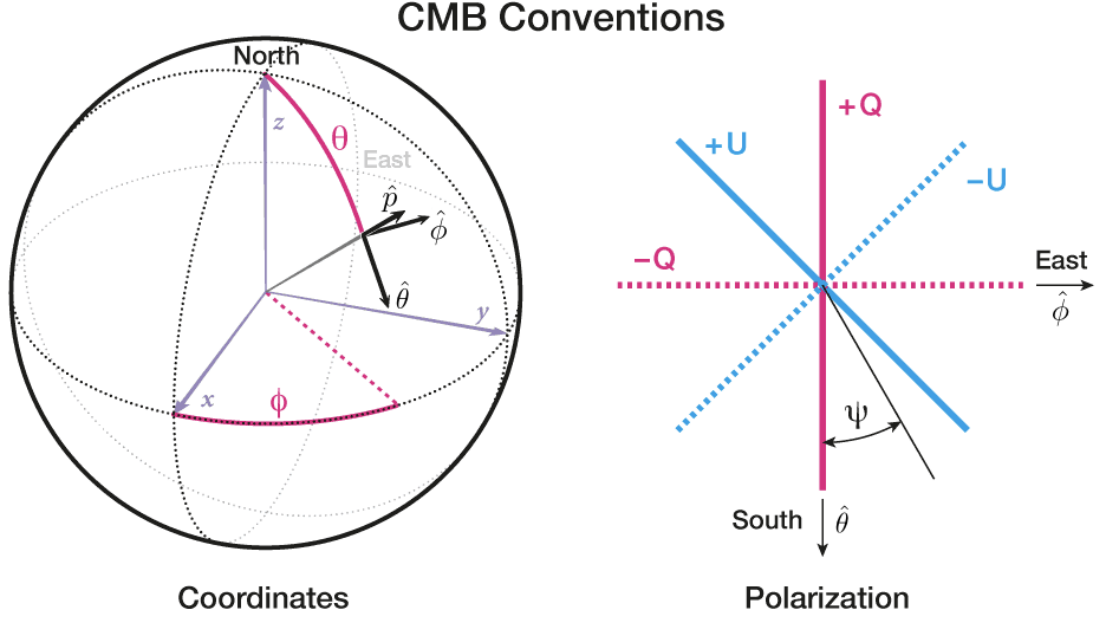
CMB Conventions

Coordinates

Polarization

Figure 2. Figure showing the sign conventions of Stokes parameters Q and U used by the CMB community. In this figure, ψ is the angle between the antenna basis base unit vector $\hat{\theta}'$ and $\hat{\theta}$. Positive Q if the polarization vector is aligned with $\hat{\theta}$ (North-South direction), negative Q if the polarization vector is aligned with $\hat{\phi}$ (East-West direction), positive U is aligned with $(\pm(\hat{\phi}+\hat{\theta})/\sqrt{2})$ (North/West-South/East direction), and negative U is aligned with $(\pm(\hat{\phi}-\hat{\theta})/\sqrt{2})$ (North/East-South/West direction). The rightmost panel of this figure corresponds to an observer looking towards Earth. This figure is adapted from one that was found on NASA's LAMBDA website and was originally published in [11]

Many CMB experiments use polarization sensitive bolometers (PSBs) as detection devices, which are pairs of bolometers placed at the focus of the optical chain. By construction, each bolometer is more sensitive to a particular orientation of incoming electric fields. Given a PSB consisting of a pair of detectors (a, b) whose polarization sensitive axes are aligned at angles ζ and $\zeta - 90°$ with respect to the antenna basis unit vector $\hat{\theta}'_0$, we can define beam center polarization unit vectors for each detector as

$$\hat{e}_{a,\parallel} = \cos(\zeta)\hat{\theta}'_0 + \sin(\zeta)\hat{\phi}'_0 \tag{3.3}$$

$$\hat{e}_{a,\times} = \sin(\zeta)\hat{\theta}'_0 - \cos(\zeta)\hat{\phi}'_0 \tag{3.4}$$

$$\hat{e}_{b,\parallel} = \sin(\zeta)\hat{\theta}'_0 - \cos(\zeta)\hat{\phi}'_0 \tag{3.5}$$

$$\hat{e}_{b,\times} = -\cos(\zeta)\hat{\theta}'_0 - \sin(\zeta)\hat{\phi}'_0. \tag{3.6}$$

The polarizing properties of an antenna can be obtained by combining the concept of a beam with the Mueller matrix formalism. Mueller matrices are widely used to quantify the effect that an optical element has on the polarization state of incoming light. This process is modeled by the multiplication of 4×4 matrix $\mathbf{M}$ with a Stokes vector S_{in}, such that the Stokes vector of radation that has interacted with the optical element becomes

$$S_{\text{out}} = \mathbf{M} S_{\text{in}}. \tag{3.7}$$

As described in the work of [20] and [18], antennas can be modeled using Mueller matrices. PISCO uses the formalism presented in [18], since it is more suitable to be applied to CMB experiments. We note the original paper names "beam Mueller fields" to this extended definition of a antenna beam. To emphasize the multi-dimensional nature of this mathematical entity, in this work we refer to it as a beam tensor, or *beamsor* for short.

A beamsor can be interpreted as a field of Mueller matrices such that for each direction (ρ, σ), there is an associated Mueller matrix that quantifies the coupling between the antenna and a Stokes vector coming from (ρ, σ). We will denote a beamsor by letter $\mathbf{B} = \mathbf{B}(\rho, \sigma)$. At every antenna basis direction, $\mathbf{B}$ is a 4×4 matrix in the form

$$\mathbf{B}(\rho, \sigma) = \frac{1}{\tilde{\Omega}} \begin{bmatrix} B_{TT} & B_{QT} & B_{UT} & B_{VT} \\ B_{TQ} & B_{QQ} & B_{UQ} & B_{VQ} \\ B_{TU} & B_{QU} & B_{UU} & B_{VU} \\ B_{TV} & B_{QV} & B_{UV} & B_{VV} \end{bmatrix} \tag{3.8}$$

where $\tilde{\Omega}$ is a normalization factor given by

$$\tilde{\Omega} = \int_{4\pi} B_{TT}(\rho, \sigma) \, \mathrm{d}\Omega \tag{3.9}$$

and the elements of $\mathbf{B}$ are defined in the work of [18]. Note that in the case of no cross polarization and perfectly matched beams, the beamsors reduce to the Kronecker product

$$\mathbf{B}(\rho, \sigma) = b(\rho, \sigma) \otimes \mathbf{I} \tag{3.10}$$

where $\mathbf{I}$ is an identity matrix.

4 Measuring the sky with polarization sensitive antennas

4.1 Continuous case

In order to model the process by which a polarization sensitive detector transforms electromagnetic radiation into current or voltage, we used the formalism described in [13]. In Mueller matrix space, a partially polarized, total power detection device corresponds to the following row-vector

$$D(\zeta, \epsilon, s) = \frac{s}{2} \left[(1 + \epsilon), (1 - \epsilon) \cos(2\zeta), (1 - \epsilon) \sin(2\zeta), 0 \right] \tag{4.1}$$

where $1 - \epsilon$ is the polarization efficiency, s is the voltage responsivity of the detector and ζ was defined in §3. The process of taking a total power measurement on a Stokes vector S^i can then be modeled as a dot product which, using Einstein's summation convention, yields

$$d = D_i S^i. \tag{4.2}$$

Stokes vector S^i is, in turn, the convolution between the antenna beamsor and the polarized sky. The complete expression describing the measurement taken by a linearly polarized, total power detector coupled to an antenna pointing along $\hat{p}$ with position angle ψ_0 becomes

$$d(\bar{q}_0) = \int_{4\pi} D_i(\chi, \epsilon, s) \Lambda^i{}_l(\chi) B^l{}_j \left[\Lambda^j{}_m(-\chi) S^m \right] \mathrm{d}\Omega \tag{4.3}$$

where $(i, j) = T, Q, U, V$, and $\mathbf{B}$ is aligned with $(\hat{p}, \psi_0)$. Rotation of the detector polarization basis to the sky basis is carried out using χ in the argument to D, and by $\mathbf{\Lambda}$, which is a matrix field in the form

$$\mathbf{\Lambda}(\chi) = \begin{bmatrix} 1 & 0 & 0 & 0 \\ 0 & \cos(2\chi) & -\sin(2\chi) & 0 \\ 0 & \sin(2\chi) & \cos(2\chi) & 0 \\ 0 & 0 & 0 & 1 \end{bmatrix}. \tag{4.4}$$

4.2 Pixelated case

In order to calculate the result of equation 4.3 using a computer, we can no longer use continuous distributions, so we need to use pixelated versions of both the beamsor and sky model. Both the sky model S and beamsor $\mathbf{B}$ must then be transformed into a matrix of N_b (number of pixels in the beamsor) and N_s (number of pixels in the sky model) entries, respectively. We will denote the k-th pixel of the pixelated beamsor $\mathbf{B}$ (sky S) as $_kB$ ($_kS$). With the above in mind, we can write equation 4.3 for the pixelated case as

$$d(\bar{q}_0) = \sum_{k=1}^{N_s} {}_kD_i(\chi, \epsilon, s) \ {}_k\Lambda^i{}_l(\chi) \ {}_kB^l{}_j \ {}_k\Lambda^j{}_m(-\chi) \ {}_kS^m. \tag{4.5}$$

where $\mathbf{B}$ has been properly re-pixelated via interpolation, so as to keep track of the actual position of the beam on the sky according to $\bar{q}_0$ using the equations presented in Appendix A. It is worth noting that this expression operates on a pixelated sky, so information at angular scales that are smaller than a sky pixel is lost.

5 PISCO

The **PI**xel **S**pace **CO**nvolver (PISCO) is a tool with the capability of generating synthetic Time Ordered Data (TOD) provided a model for the beamsor, the scanning strategy of the mission and a sky model. In this section, we present a pathfinder implementation of PISCO that exploits the massively parallel architecture of modern GPU systems.

5.1 General description

PISCO is the software tool in charge of generating mock TOD given a beamsor, a sky model and a scanning strategy. A diagram showing the general workings of PISCO is shown in Figure 3. PISCO receives as input a sky model in the form of 4 maps representing Stokes parameters I, Q, U and V, a beamsor, pointing and focal plane information. PISCO stores the beamsor elements and sky model as HEALPix (see [10]) maps. HEALPix was chosen because it is widely used among the CMB community, and because it naturally handles the closed surface topology of the sphere. HEALPix also provides equal area pixels, which is a desirable feature when computing convolution in pixel space. The focal plane specifications are only needed if multiple detectors are being included in the pointing stream, as PISCO needs the the angle ζ of each detector to compute equation 4.5. All the inputs are sent to the TOD generation function, which returns the data streams. At this point, the data can either be saved to disk or sent to a map-making code. This last step is preferred as, usually, input-output operations are time consuming. Finally, maps can be analyzed using external tools to calculate the power spectra.

5.2 Implementation using CUDA

GPUs allow for substantial acceleration of algorithms that perform a large amount of independent operations. TOD generation using equation 4.5 presents an optimal application case because all operations are independent of each other. In this work, we used the Compute Unified Device Architecture framework from NVIDIA to implement the TOD generation routine. The reader is referred to [24] for an excellent description of CUDA and associated capabilities.

To better understand how the parallelism in 4.5 can exploited, consider the process of synthesizing N_T measurements using a CUDA grid of B blocks and T threads. Consider each
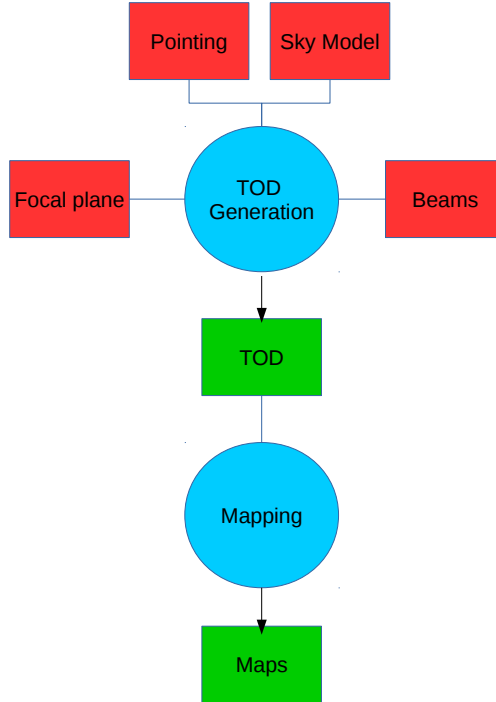
Figure 3. Basic flow of a typical PISCO simulation pipeline. Red polygons show the required user input. PISCO uses this input and produces TOD (green polygon). This TOD stream is calculated using equation 4.5 for all pointing directions. TOD can then by sent into a mapper and, finally, to a power spectra estimator tool. PISCO does not compute pointing nor produces maps from TOD by itself; these tasks are left to external programs.

measurement to have an associated pointing $\bar{q}_t$ with $t = 0..N_T$. PISCO performs a double parallelization scheme: the "slow" loop ($L1$) scans the pointing stream and associates every block to a pointing $\bar{q}_t$. A second, "faster" loop ($L2$), iterates over a list of pixels, which correspond to sky pixels that are "inside" the beamsor extension. This list of pixels is constructed in advance and then transferred to the GPU. $L2$ executes T operations in parallel. Great care was taken to ensure no race conditions arise when multiple threads try to read (write) from (to) the same memory address. As every block executes T convolution operations in parallel, and the CUDA grid runs B simultaneous blocks, the parallelism is $B \times T$. Furthermore, if G GPUs are available, the computation can be distributed among them, increases the parallelism to $G \times B \times T$. A graphical description of this process is shown in Figure 4.

5.3 Performance

5.3.1 Benchmark results

To gain insight on the performance of the algorithm, we performed a simple benchmark where a single PSB scanned the whole sky with a Gaussian beam of FWHM= 1.5°. We restricted the benchmark to Gaussian beams only but emulated the presence of sidelobes by increasing the number of sky pixels involved in the convolution on every run. The benchmark on timing 2 detectors with the same beams scanning the complete sky at 3 different beam orientation angles
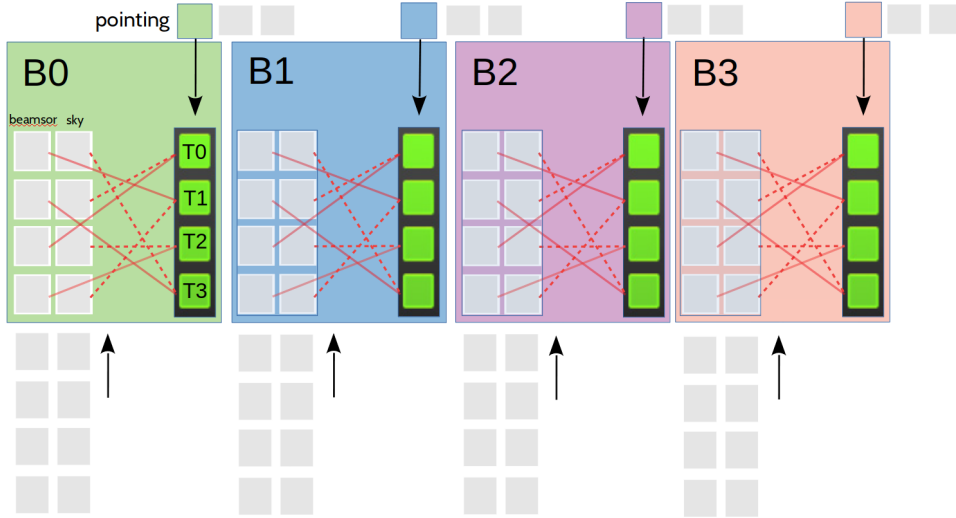
Figure 4. Parallelization scheme. This figure shows the case of PISCO executing in 4 blocks ($B = 4$), with four threads per block ($T = 4$). Arrays with beamsor and sky elements are at the bottom. Each block has access to four beamsor and sky pixels (gray boxes inside colored boxes) and one pointing entry (colored small boxes) at a time. Green boxes represent the multiplication process of a single beamsor pixel with a single sky pixel. This includes rotating the sky pixel to the detector polarization basis, and computing the re-pixelization of B at the corresponding coordinates. Solid and dotted red lines represent the complex memory access pattern generated by this process. Every thread within a block writes its result to shared memory space. When a thread finishes its computation, it waits until all threads have finished and a reduction on the shared memory space is performed across all blocks. This process is repeated for every pointing. At the end of the procedure, each block has computed the convolution of a beamsor with the sky for a particular pointing, and every shared memory space of the block has the corresponding result. These results are collected into the GPU global memory, which is then transferred back to CPU (host) memory.

($0°$, $45°$ and $90°$). The pointing of every detector was set to aim at the center of every sky pixel, effectively setting the number of samples in the TOD to 3 times the number of pixels on the sky, per detector. We used a polarized CMB map of NSIDE=128 (196608 pixels) as input, which set the number of samples in the synthetic TOD to 589824. Conversely, the NSIDE parameter of the beam was set to 512. The test was ran on a single GTX 1080 card and a node equipped with two Intel Xeon E5-2610 processors (10 physical cores and 20 threads per processor) and 256 GB of DDR4 RAM. Unfortunately, the current code architecture does not allow for a simple way of measuring performance in FLOPS, which is a challenging task on its own given the TOD generation routine performs both integer and floating point mathematical operations. For this reason, we report execution wall-time as a metric for performance.

Table 1 shows the scaling of wall-time with ρ_{max}, which was found to be roughly quadratic. Auxiliary runs showed that the execution scales linearly with the number of samples. The behavior of this scaling is expected from the architecture of the algorithm (see Figure 4), and can be ameliorated by using a distributed computing architecture with multiple GPUs. Another free parameter, the `NSIDE` parameter of the beam, was found to have a minor effect on execution time. The degradation caused by using a finer beam is believed to be a consequence of the GPU having less free memory to store the evaluation grid, which reduces the ability fo calculate a larger amount of parallel convolutions.

5.3.2 Discussion and future improvements

Algorithms like `beamconv` (see [8]), or even the `smoothing` routine present in the `healpy` package, work in ℓm space, meaning their execution times are much faster for this particular case where the
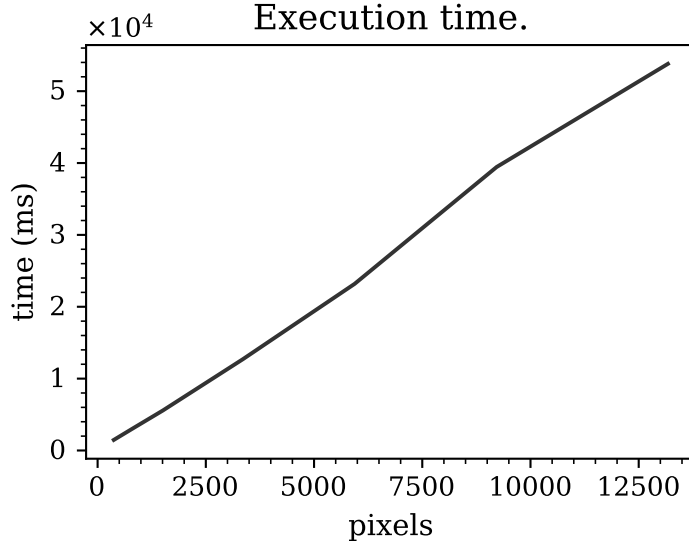
Figure 5. Plot showing data from table 1. The knee at around 5000 pixels is caused by the chunking mechanism that is turned on when there is no more GPU RAM available to store the evaluation grid. The scaling of wall-time with the amount of pixels involved in the convolution scales as a power law, as expected from the nature of the algorithm.

$\rho_{\max}$ (°)	Pixels	Wall time (ms)
5.0	374	1471.41
7.5	832	3135.19
10.0	1506	5560.25
15.0	3360	12719.56
20.0	5938	23190.68
25.0	9218	39447.70
30.0	13174	53800.74

Table 1. Table showing wall-times for single detector whole-sky convolution. $\rho_{\max}$ corresponds to the "cut-off" angle that is taken into account by the core convolution algorithm. The central column corresponds to the maximum number of sky pixels involved in the convolution. Third column corresponds to wall time, including the assembly of the beam interpolation grid, copying memory between the host and the GPU, as well as the wall-time of the main convolution routine. We note that, because of the limited amount of RAM in the GPU, runs with $\rho_{\max} > 15°$ were performed in blocks in a purely serial manner.

beam is highly symmetric. It is worth noting that, in theory, the nature of the core algorithm allows to include other features in the simulation (bema ghosting, sharp sidelobes or time-dependent phenomena) at a relatively small computational cost. We believe this makes PISCO a good complement to other software tools that perform similar tasks.

The current implementation must calculate the list of sky pixels involved in each convolution, for all pointing directions, before the CUDA routine is launched. While the wall-time associated with this operation is modest, the result must be kept in memory and transferred to the GPU, so that the associated buffer quickly becomes too large to be held in the VRAM. Currently, PISCO handles this situation by performing the generation of TOD in blocks to avoid memory overflow. In the test machine, computing and transferring the lists of pixels can take up to 13% of the *overall* simulation wall-time. A solution to this problem has already been devised and will be implemented in future releases. Another drawback of the current implementation is the use of global memory to hold the beam tensor elements. Future releases will exploit data locality by making use of the CUDA texture memory pipeline (see [24] and [3]). Finally, while the

current implementation of PISCO was designed to execute in multiple GPU nodes, significant coding effort is required to provide the user with an easy to use interface. Experiments were performed emulating a multi-node system by making PISCO use all 3 GPUs of the machine. These tests showed an almost linear increase in performance, but more work is required in order to find the knee of the curve between performance and available GPUs.

6 Code validation

To validate the correctness of PISCO, we performed two sets of tests: a mock observation of a (polarized) point source and a simulation of an ideal CMB observation. Results from these tests were compared against the `healpy.smoothing` routine, a Python wrapper around HEALPix routines, which calculates the convolution of a polarized sky with a circularly symmetric Gaussian beam in $a_{\ell m}$ space. For the purposes of this section, we will consider the output of `smoothing` to be exact.

6.1 Point source observations

The simulated observation of a polarized point source was accomplished by the following steps

- Build a beamsor with off-diagonal elements set to zero. Every B^i_i element corresponds to a circular Gaussian beam with FWHM of $1.5°$.

- For simplicitly, we used a PSB with $s = 1$ and $\epsilon = 0$ for both detectors.

- Build a mock sky, with a single non-zero pixel at coordinates (θ_k, ϕ_k). Three cases were run: unpolarized, pure Q polarization and pure U polarization.".

- Set up a raster scan around (θ_k, ϕ_k) for a detector with $\zeta = 0$. Note that, in order to have full polarization coverage, the raster scan is repeated 3 times with angles $\psi_0 = 0°, 45°, 90°$.

- Make maps of TOD generated by PISCO.

- Compare the result of applying `smoothing` to the single pixel map using the same beam model.

6.1.1 Results

Results from this validation test are shown in Figure 6. The results show that the flux is preserved to better than 0.2%. For the `NSIDE` 256 sky used in this test, doubling `NSIDE` of the beam from 1024 to 2048 does not improve the preservation of the flux significantly (from 0.2% to 0.04%) at the cost of quadrupling the amount of memory required to store the beamsor, while using a lower `NSIDE` for the beam degrades this considerably to 0.8%. We conclude that a 4:1 beam to sky `NSIDE` ratio is sufficient. We also checked for systematic effects driven by the finite machine precision of the computations, and found that leakage from temperature to polarization was consistent with zero to machine precision. The maximum residual in the P to P leakage is on the order of 0.1%. PISCO is also able to correctly account for intra-beam variations of the position angle χ.

6.2 Ideal CMB experiment

6.2.1 Description

The simulation of an ideal CMB experiment was accomplished by the following:

- Build a beamsor with off-diagonal elements set to zero. Every B^i_i element corresponds to a circular Gaussian beam with FWHM of $1.5°$.
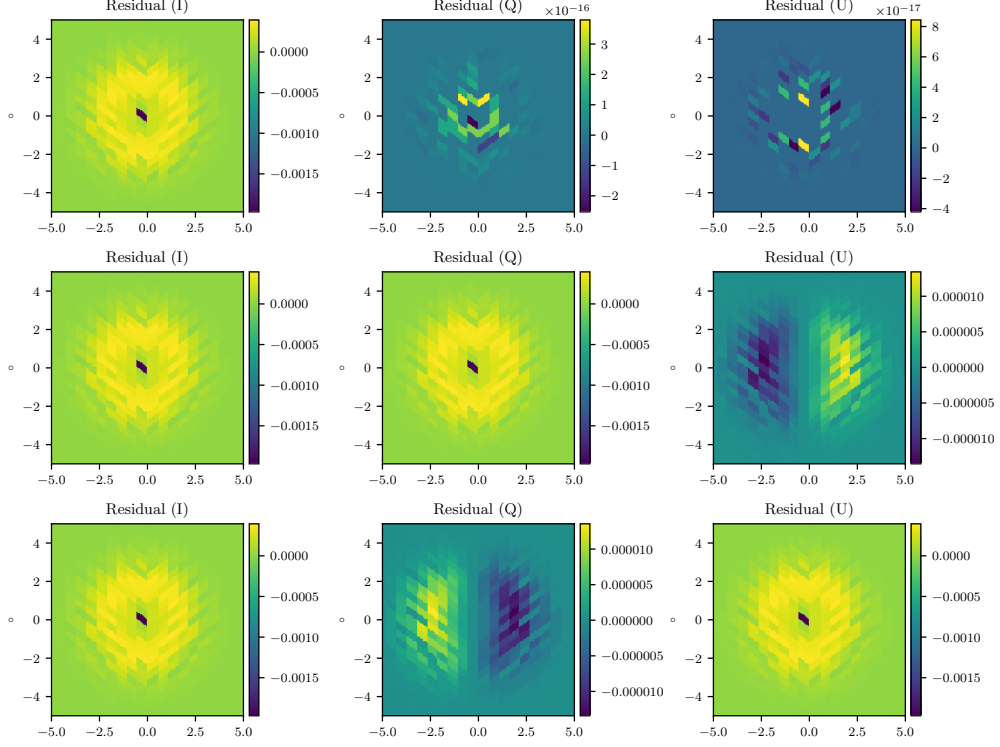
Figure 6. Plots showing the result of differencing a map with a point source convolved with a Gaussian beam using `smoothing` and the map generated from PISCO TOD. The input map used HEALPix pixelization with `NSIDE = 256`, while the beamsor resolution was set to `NSIDE = 1024`. The Gaussian profile used for the beamsor had a FWHM of 1.5°. All point sources were located at 45° declination. The color scale is normalized to 1, which is also the amplitude of the source. From top to bottom: residuals for the case of a point source with Stokes vector $S = (1, 0, 0, 0)$, $S = (1, 1, 0, 0)$ and $S = (1, 0, 1, 0)$, respectively.

- For simplicitly, we used a PSB with $s = 1$ and $\epsilon = 0$ for both detectors.

- Build mock CMB whole sky maps with a tensor-to-scalar ratio $r = 0.0$.

- Set up a scanning strategy to visit each pixel center at 3 different position angles $\psi_0 = 0°, 45°, 90°$.

- Make maps of TOD generated by PISCO.

- Compare spectra generated from the maps with spectra of the input maps.

6.2.2 Sky model

The input sky maps were generated using a combination of CAMB (see [14]) to generate C_ℓ and `synfast` to generate maps from the C_ℓ. The cosmological parameters used by CAMB are consistent with those reported by the *Planck* satellite collaboration (see [22]). This procedure returns 3 CMB anisotropy maps, one for each Stokes parameter. The CMB is not expected to have Stokes V polarization, so this field was explicitly set to zero. CAMB was configured to return a CMB with no primordial B-modes ($r = 0$) and no lensing, as this last effect is expected to transform E-modes to B-modes. The resulting B-mode power spectrum is effectively zero at all angular scales. No foreground or other sources were added on top of the simulated CMB. All maps used for this simulation us the `HEALPix` pixelization scheme and were generated at a resolution parameter `NSIDE= 512`.
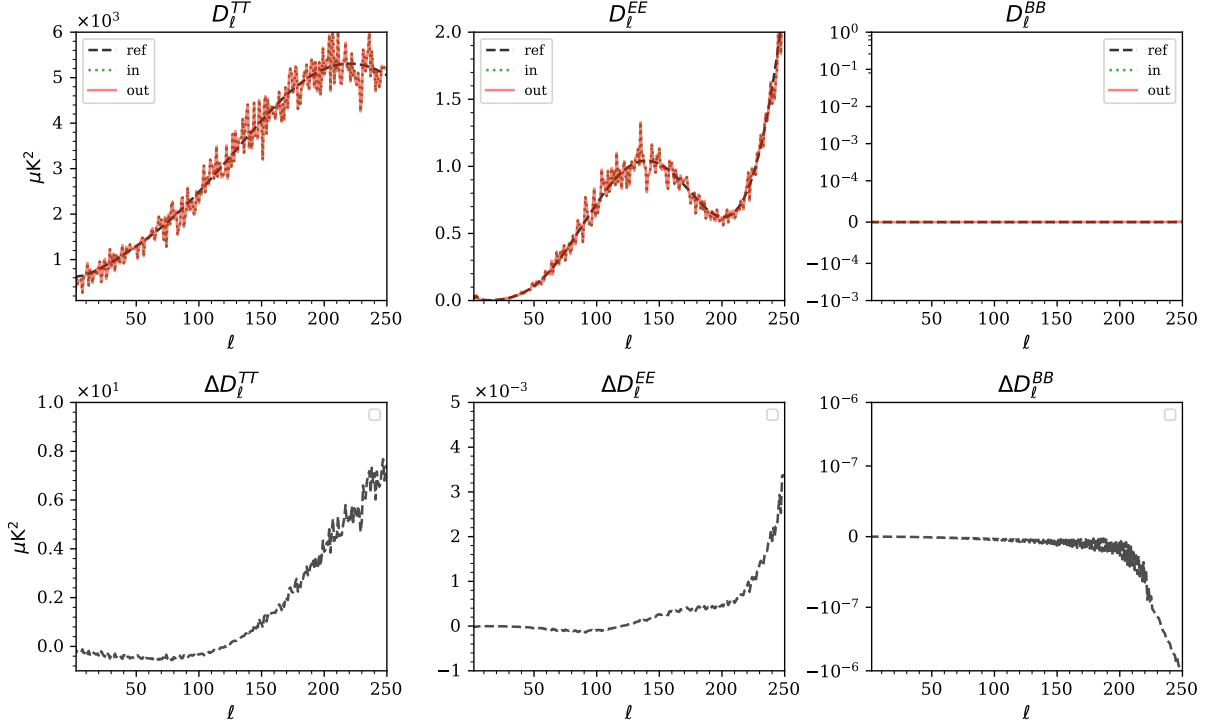
Figure 7. Upper plot: power spectra from PISCO generated TOD ("out" label) for the whole sky CMB test. D_ℓ used to generate the input maps are the black, dashed curve ("ref" label). The input sky corresponds to a CMB with $r = 0.0$, and its power spectra is plotted in dotted green ("in" label). Scale of the y-axis is μK^2 for all three plots. The scaling of the y-axis is linear for TT and EE, but semi-logarithmic for BB. Visual inspection shows excellent agreement between PISCO and the input spectra, with no apparent leakage from E-modes to B-modes or from temperature to polarization. Bottom: difference between power spectra of PISCO generated TOD and the power spectra of the input map. Residuals in TT, EE and BB reach no more than $1\,\mu K^2$, $0.004\,\mu K^2$. and $-10^{-6}\,\mu K^2$, respectively.

6.2.3 Scanning strategy and beam

The pointing stream was built such as to produce an output map of `NSIDE`= 128 out of a sky of `NSIDE`= 512. The goal of this mismatch between pointing and input sky resolution is provide a more realistic simulation as, in reality, the input sky is not pixelated at all but it is the pointing stream that cannot be recorded continuously. For that matter, we used as pointing every pixel position of a HEALPix map with `NSIDE`= 128, effectively sampling the input sky on 1/16th of its pixels. Every pixel was observed at its center, which is an important requirement that ensures the intra-pixel coverage does not affect the estimation of the power spectra at high ℓ (see Appendix B on [23]). Since only three hits per pixel at different values of χ are required to recover the polarization field of the CMB, the scanning was generated for a single detector with a polarization sensitive angle $\zeta = 0$. Finally, the beam was set to be a circularly symmetric Gaussian with FWHM of 1.5° and pixelated as a HEALPix map of `NSIDE`= 2048.

6.2.4 Power spectra

Power spectra were calculated using `anafast`. No further post-processing of the power spectra was needed given that this simulated observation covers the whole sky, and hence no masking effects arise. The power spectra corresponding to maps that were generated using PISCO TOD were corrected by dividing by the equivalent beam transfer function of a circular Gaussian beam of FWHM 1.5°.

6.2.5 Results

The main result of this simulation is shown in Figure 7. A single simulation took less than 5 seconds on the testing machine. We report no indications of leakage from temperature to polarization, nor from E-modes to B-modes. It is worth noting that this process was repeated using several realizations of roughly the same cosmology, but with varying values of r. We found no evidence of leakage in any of these cases. It appears to be a tendency on the residuals to become larger at smaller angular scales.

6.3 Ideal CMB experiment with imperfect pointing

The simulation described above used pixel centers as the telescope pointing. In an effort to provide more realism to the simulation, we dropped the constraint on the pointing and performed a similar simulation to the one described in 6.2 by adding random offsets to the pointing, with respect pixel centers, both in Right Ascension and declination as

$$\phi_{i,\,\text{new}} = \phi_i + \frac{U(f\Omega)}{\sin\theta_i} \tag{6.1}$$

$$\theta_{i,\,\text{new}} = \theta_i + U(f\Omega) \tag{6.2}$$

where $U(a)$ returns a uniformly distributed random number between -0.5 and 0.5, f is scaling factor and Ω is the average pixel size of a HEALPix map which, for `NSIDE` 128, becomes $0.45°$. For the purposes of this test, f was set to 0.1.

Results from this test are summarized in Figure 8. We observe that the discrepancy between power spectra increases roughly an order of magnitude when random offsets are introduced into the pointing. Another effect is the appearance of a spurious B-mode signal. To explore the origin of this artifact, we ran another, similar simulation using an unpolarized CMB as input. These results (see Figure 9) point to that the effect we see on **??** might be E-mode to B-mode leakage. We believe the origin of this leakage is related to an uncompensated coupling of intra-pixel gradients into the map-making process. A more detailed description of this phenomena was given in [23].

The hypothesis of intra-pixel gradient coupling was validated against another, similar simulation to the one described at the beginning of this section, with the notable difference that it was ran using *symmetric* random offsets with respect to pixel centers; because gradients at the pixel scale are dominant in Right Ascension and declination, adding a negative offsets of the exact same magnitude to every pointing should, in principle, suppress the observed leakage. Results from this simulation (see 10) show that, using symmetric random offsets, the spurious B-mode signal is suppressed around 4 orders of magnitude, which supports the hypothesis of this effect being E-mode to B-mode leakage caused by the imperfect pointing offsets. It is worth to note that symmetrizing the offsets also brings down the residuals of the temperature and E-mode power spectra to levels comparable to those shown on Figure 7.

Figure 10 shows that symmetrizing the offsets indeed attenuates the leakage and improves the discrepancy between the input and output power spectra shown in Figure 8.

7 A more realistic CMB experiment

The tests performed in §6.2 correspond to an idealized case. In this section, we show results for a simple, but more realistic, application of PISCO. The focus of this section is on demonstrating that the implementation of the model presented in 3 and 5 is able to reproduce the expected effect of pointing and beam mismatch, which is T to P leakage (see [18]), and uneven intra-pixel coverage, which is P to P leakage (see [23]). As in the previous section, we did not include other systematic effects like gain imbalance, detector efficiency, cross-polarization responses and far sidelobes.
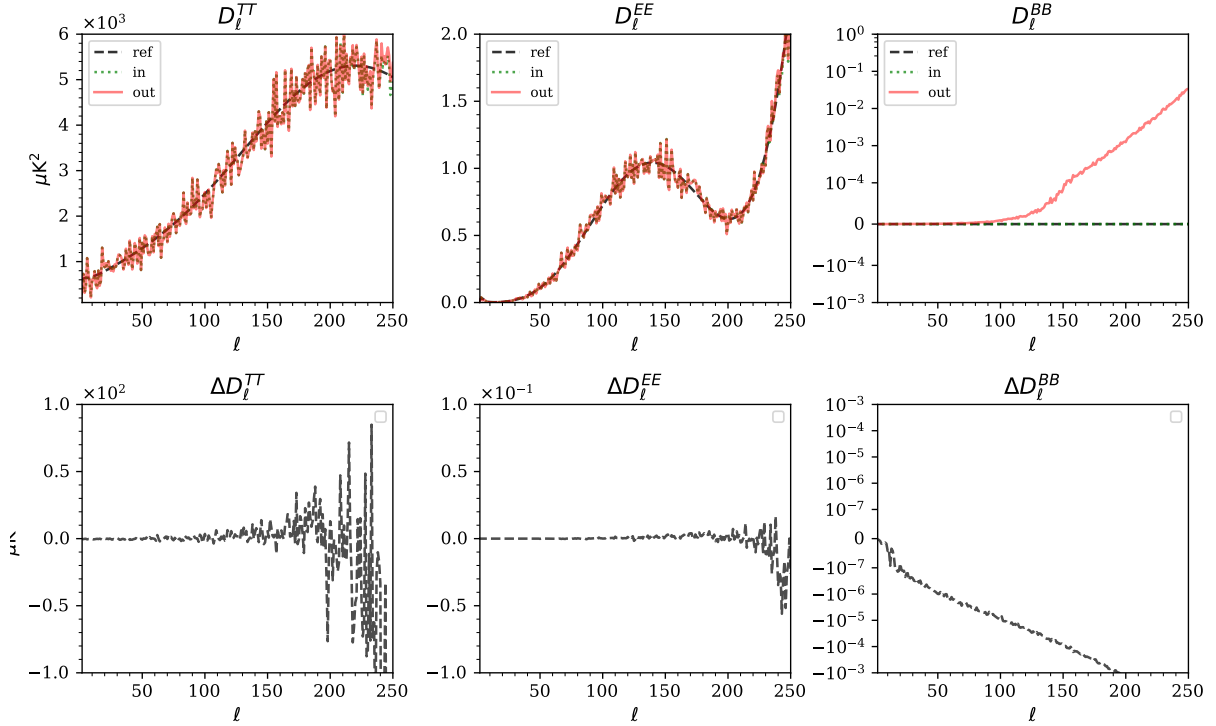
Figure 8. Upper plot: power spectra from PISCO generated TOD ("out" label) for the whole sky CMB test. D_ℓ used to generate the input maps are the black, dashed curve ("ref" label). The input sky corresponds to a CMB with $r = 0.0$, and its power spectra is plotted in dotted green ("in" label). Scale of the y-axis is μK^2 for all three plots. The scaling of the y-axis is linear for TT and EE, but semi-logarithmic for BB. Bottom: difference between power spectra of PISCO generated TOD and the power spectra of the input map. The spurious B-mode signal reaches $0.1\,\mu K^2$.

7.1 Description of the simulations

Since designing such an experiment from scratch is a challenging task, we turned to simulating an ongoing mission, the Cosmology Large Angular Scale Surveyor, CLASS. CLASS aims at characterizing the CMB anisotropy field at large angular scales, particularly the power spectra of B-modes and E-modes, looking for evidence of inflation. While the experiment is composed of 4 telescopes, the simulation focuses on the one observing at the lowest frequency (38 GHz), the Q-band receiver, which has a 1.5 degree beam. This decision was taken for computational reasons, mainly because Q-band has lower detector count compared to higher frequency receivers. We note that CLASS uses modulation techniques to increase its sensitivity to CMB polarization. The effects of modulation related systematics have been described elsewhere ([16]). For a more detailed description of CLASS, the reader is referred to [12], [9] and [2].

7.1.1 Sky model

To generate the maps for this simulation, we followed a similar procedure to the one described in §6.2.2. The main difference is the addition of a temperature only CMB, which was used to check for T to P leakage caused by effects that were not present in the last test presented in §6 All maps use the `HEALPix` pixelization with an `NSIDE` parameter of 128.

7.1.2 Pointing

The scanning strategy of CLASS consists of constant elevation scans (CES). Elevation is kept at $45°$ while the telescope rotates $720°$ in azimuth at 1 degree per second. Under normal survey conditions, the telescopes scan nearly 24 hours a day. The boresight is rotated from $-45°$ to $+45°$ by $15°$ per day on a weekly schedule. This scanning strategy, in combination with the large
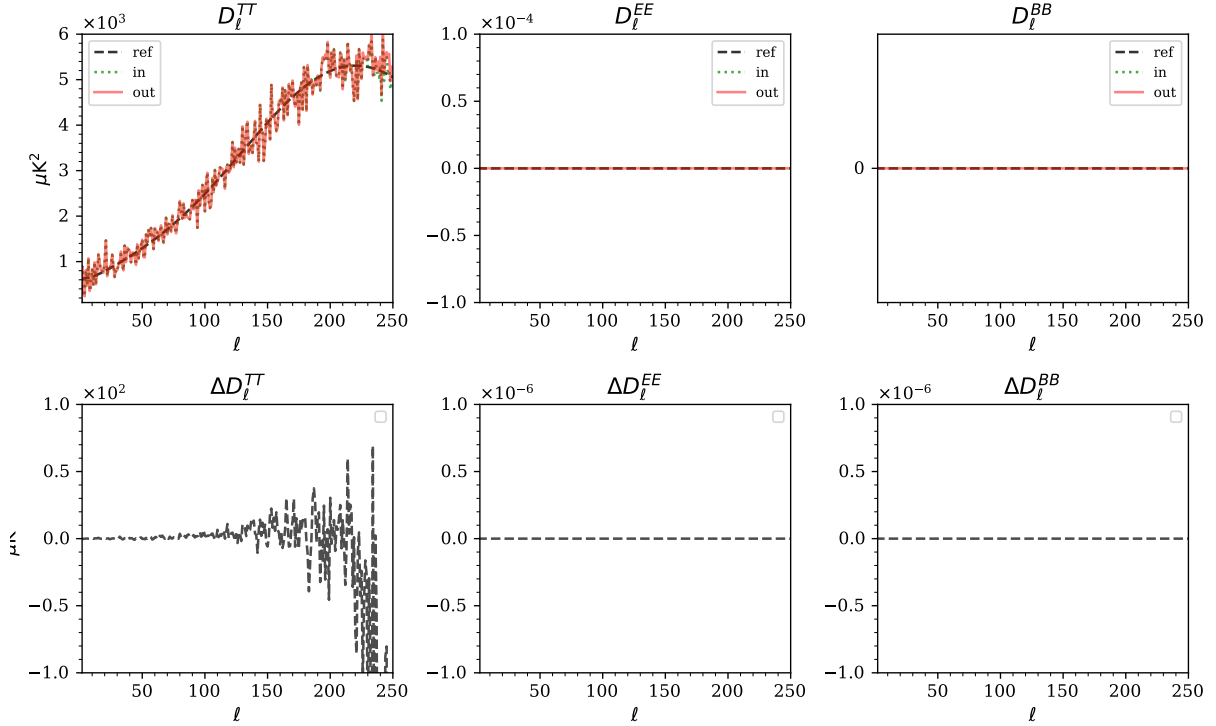
Figure 9. Upper plot: power spectra from PISCO generated TOD ("out" label) for the whole sky CMB test. D_ℓ used to generate the input maps are the black, dashed curve ("ref" label). The input sky corresponds to a CMB with $r = 0.0$, and its power spectra is plotted in dotted green ("in" label). Scale of the y-axis is μK^2 for all three plots. The scaling of the y-axis is linear for TT and EE and BB. Bottom: difference between power spectra of PISCO generated TOD and the power spectra of the input map. This plots shows no signs of temperature to polarization leakage.

CLASS field of view results in the telescopes covering more than 70% of the sky. In addition, because of the boresight rotation, only seven days are needed to provide excellent position angle coverage. While CLASS records data 200 times per second, the pointing streams were generated at 20 Hz. Down-sampling by a factor of 10 results in a ten-fold decrease in computation time with the median number of hits per pixel still being on the order of thousands. Even with this significant reduction, the pointing stream contained more than 870 million samples.

Equatorial coordinates of every detector were computed from the horizontal coordinates produced by the scanning strategy and the beam center offsets of every detector from the center of the array. Representative beam center offsets for the Q-band receiver were provided by the CLASS collaboration. Two streams were generated by considering detector pairs to have matched or mismatched offsets. The case of matched offsets was simulated by forcing each pair to share the same beam center offsets, which in turn were calculated as the average of the individual pair offsets.

7.1.3 Beamsor model

The CLASS collaboration also provided us with representative main beam parameters. The main beam parameters correspond to FWHM in the East-West direction (FWHM_x), FWHM in the North-South direction (FWHM_y) and the rotation angle of the major axis of the corresponding elliptical profile. The simplicity of the beams allows a further speed-up in the computation by restricting the convolution to a $5°$ disc around the beam center. This value was chosen as, for a unit normalized Gaussian beam, a pixel that is $5°$ away from the centroid of the $1.5°$ FWHM beam of the CLASS Q band receiver has a value of $\approx 10^{-14}$, roughly the limit of double precision arithmetic. All beamsors were pixelated using NSIDE = 512. The finite resolution
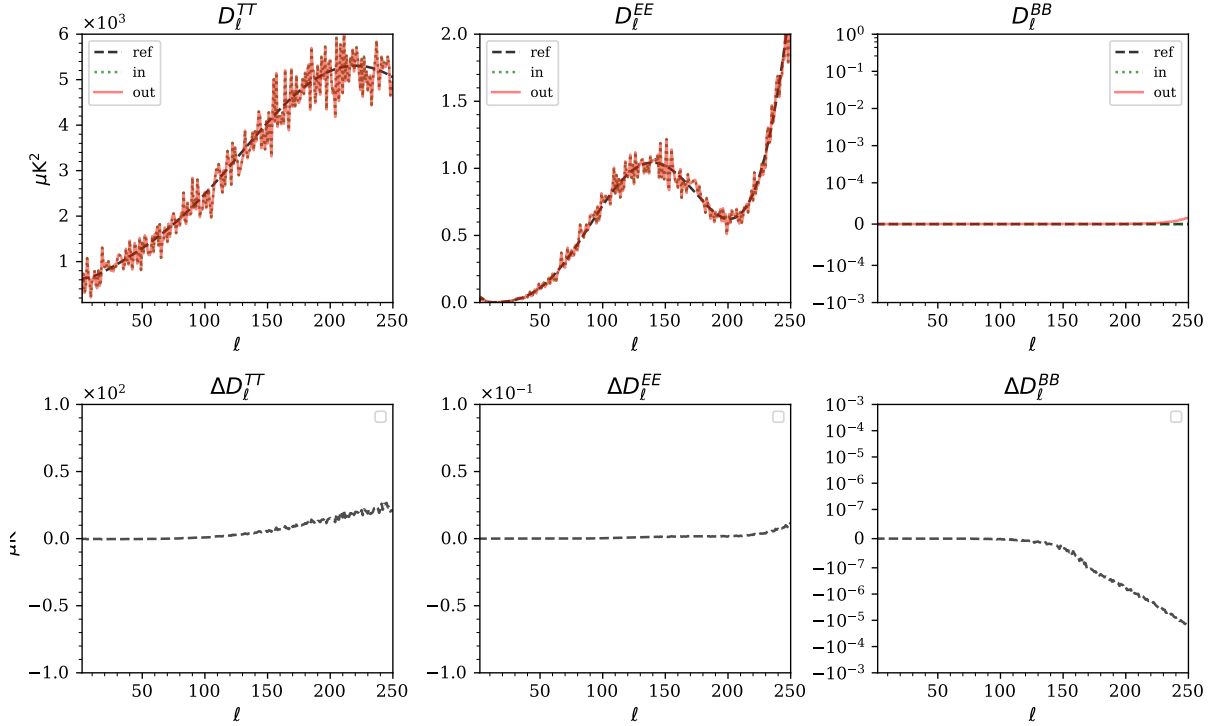
Figure 10. Upper plot: power spectra from PISCO generated TOD ("out" label) for the whole sky CMB test. D_ℓ used to generate the input maps are the black, dashed curve ("ref" label). The input sky corresponds to a CMB with $r = 0.0$, and its power spectra is plotted in dotted green ("in" label). Scale of the y-axis is μK^2 for all three plots. The scaling of the y-axis is linear for TT and EE, but semi-logarithmic for BB. Bottom: difference between power spectra of PISCO generated TOD and the power spectra of the input map. The spurious B-mode signal reaches $10^{-5} \mu K^2$ al $\ell = 250$.

of the beamsor produces an error in the amplitude of simulated TOD that is less than 0.1% compared to analytical estimations, which is consistent with the results described in §6.

7.1.4   Power spectra and beam transfer function

Given that CLASS only covers $\approx 70\%$ of the sky, computing the power spectra of simulated maps requires the use of a tool than can handle a sky mask. For this reason, we changed the estimator from `anafast` to `Spice` through the `PolSpice` implementation (see [6]). In addition, the CLASS collaboration provided a realistic sky mask that includes the galactic plane as well as the sky outside the survey boundaries.

While the effect that smooth, circularly symmetric beams have on the power spectra is known (see [19]), beams for CLASS have non-zero eccentricity and so we need to account for the effect of this on the CMB power spectra. This is done by computing the radial profile of each beam through an analytical integration over ϕ, averaging the radial profiles of all of the beams in the array receiver and then calculating the harmonic transform of the average profile to use as the beam transfer function in deconvolving the power spectra.

7.1.5   A unified metric for describing mismatch

While it is simple to use the difference in pointing between two paired detectors to describe pointing mismatch, elliptical beam mismatch involves three quantities: the difference in the semi-major beam widths, the difference in the semi-minor beam widths and the difference in orientation of the two elliptical beams on the sky. When multiple pairs are considered, it becomes unclear how to average these parameters in order to gain insight into the degree of mismatch in the set. For this reason, it is desirable to define a metric that can be suitably
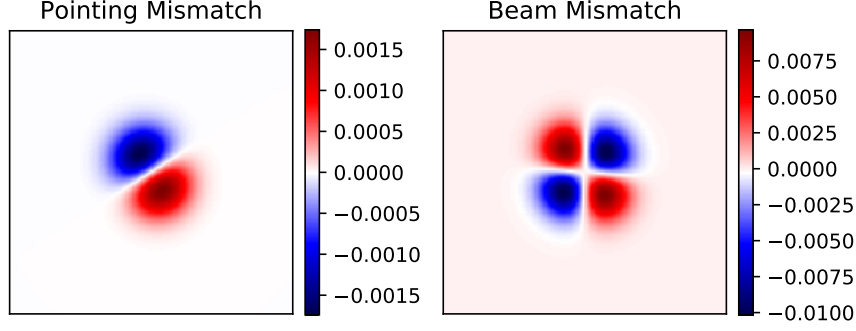
Figure 11. Example pair differenced elliptical Gaussian beams for pointing mismatch and beam mismatch. The resulting metrics are $\delta_p = 0.17\%$ and $\delta_b = 1.0\%$.

applied to more than one pair. One such metric can be derived from the difference $\Delta b(\rho, \sigma)$ in the fitted elliptical Gaussian beams for the detector pair of each PSB by considering the maximum difference expressed as a percentage of the normalized beams, namely

$$\delta_{(p,b)} = \max \left| \Delta b_{(\mathrm{p,b})}(\rho, \sigma) \right| \tag{7.1}$$

where the subscripts p and b represent the cases of pointing mismatch and beam mismatch respectively (see Figure 11). This unified metric is directly proportional to the difference in convolution weighting for each detector pair and can be meaningfully averaged over multiple pairs.

7.2 Results and discussion

7.2.1 Matched pointing and beams

For the purpose of comparison, a test was run using matched beams. This was done by averaging both the pointing offsets and elliptical beam parameters for each detector pair in the array. The results of this test are shown in the upper plot of Figure 12. In this and all subsequent plots the theoretical E-mode and B-mode spectra for a universe with $r = 0.01$ were overlaid to provide context. As expected, the result of this test is that there is no T to P leakage present.

7.2.2 Pointing mismatch

CMB experiments that rely on detector pairs are subject to leakage caused by pointing mismatch. As described in the work of [18], differential pointing between individual detectors belonging to the same PSB couples to gradients in the temperature field.

This test was performed by using the pointing offsets of the individual detectors while averaging the elliptical beam parameters for each detector pair in the array. Applying the metric described in §7.1.5 to the beams used in this simulation yielded an average value of $\delta_p = 0.42\%$ for the resulting pair differenced pointing mismatch.

The leakage caused as a result of this pointing mismatch is presented in the lower plot of Figure 12. We found that the spurious B-mode signal produced by pointing mismatch reaches $0.02 \, \mu\mathrm{K}^2$ at $\ell = 250$ at $\ell = 200$, and becomes dominant with respect to a refence B-mode spectra with $r = 0.1$ at $\ell = 160$.

7.2.3 Beam mismatch

Beam mismatch produces leakage from temperature to polarization by introducing a coupling between the beam and local quadropole-like patterns in the temperature fields (see [18])

This test was performed by using the elliptical beam parameters of the individual detectors while averaging the pointing offsets for each detector pair in the array. Applying the metric
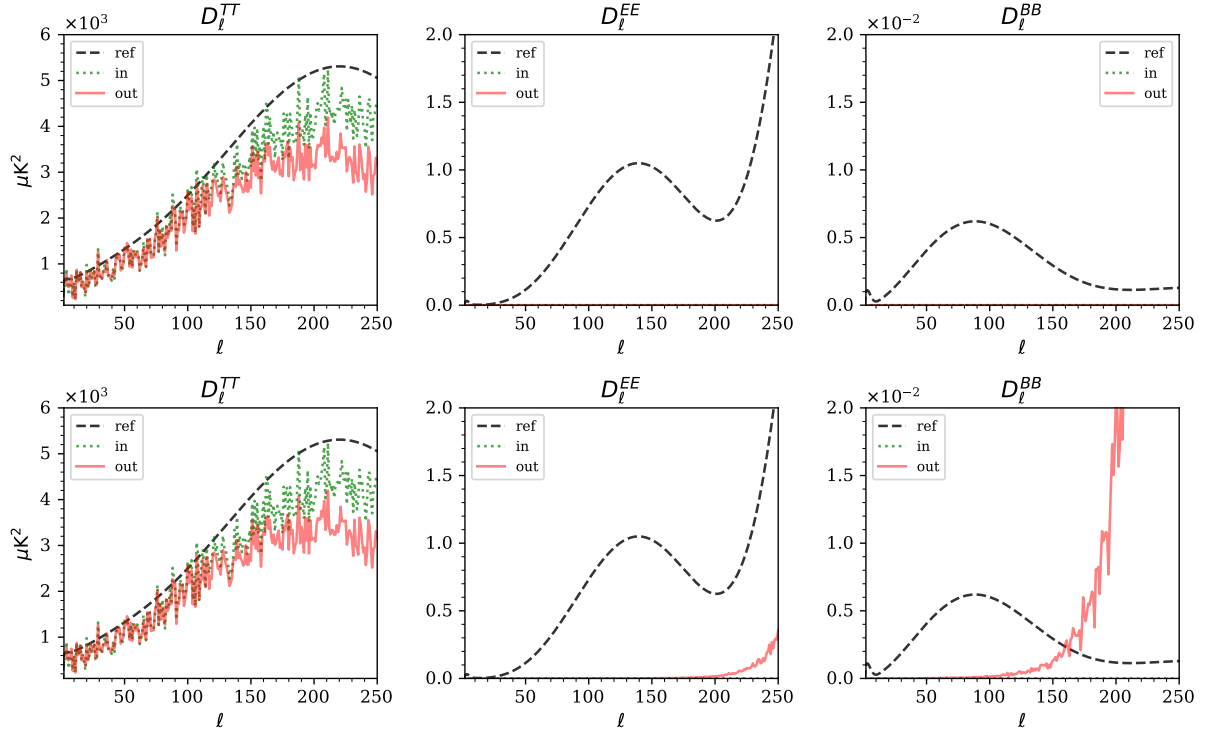
Figure 12. Resulting power spectra for a realistic simulation using matched pointing (upper figure), and mismatched pointing (bottom figure). The input CMB was unpolarized, but reference E-mode and B-mode power spectra for a CMB with $r = 0.1$ are shown using the black, dashed line. Leakage from TT to EE and BB power spectra is present for the simulations with mismatched pointing. The spurious leakage signal becomes dominant compared to reference B-modes about $\ell \approx 170$, reaching $0.02\,\mu\text{K}^2$ at $\ell = 250$.
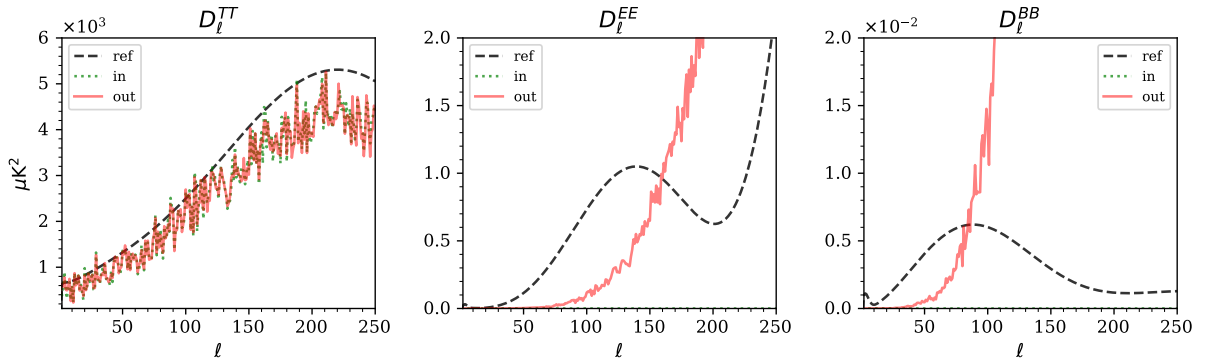

Figure 13. Resulting power spectra of a realistic simulation showing the effects of beam mismatch. Uneven intra-pixel and pointing mismatch were removed from this simulation. The input CMB was unpolarized, so that the resulting E-mode and B-mode power spectra can only be a result of T to P leakage. Reference E-mode and B-mode power spectra for a CMB with $r = 0.01$ are shown using the black, dashed line. The amplitude of the leakage signal reaches roughly $0.05\,\mu\text{K}^2$ at $\ell = 80$, dominating when compared toa B-mode power spectrum (for $r = 0.1$) above this ℓ. Similarly, the E-mode power spectra caused by leakage reaches around $0.8\,\mu\text{K}^2$ at $\ell = 160$, and dominates the signal after that angular scale.
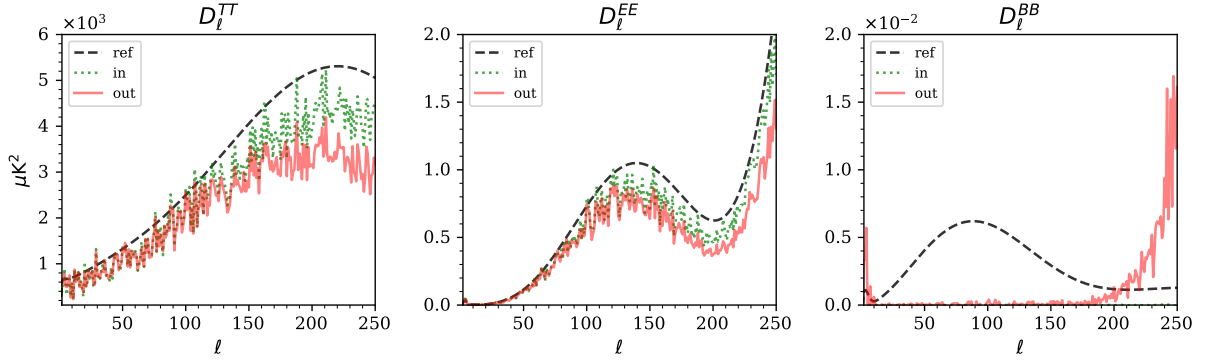
Figure 14. Resulting power spectra for the case of matched pointing with uneven intra-pixel coverage using as input a polarized CMB without B-modes. The B-mode power spectrum shows non-negligible amounts of a spurious signal not present in the input power B-mode power spectrum. Reference E-mode and B-mode power spectra for a CMB with $r = 0.01$ are shown using the purple, dashed line. The spurious B-mode spectrum reaches in the order of $1\,\mathrm{nK}^2$ at $\ell = 250$.

described in §7.1.5 to the beams used in this simulation yielded an average value of $\delta_b = 1.73\%$ for the resulting pair differenced beam mismatch.

Figure 13 shows the resulting power spectra. The leakage reaches around $0.05\,\mu\mathrm{K}^2$ at $\ell = 100$, and the spurious B-mode signal becomes dominant when compared to the theoretical spectrum of primordial B-modes for $r = 0.1$ after $\ell = 80$. We note that leakage also becomes dominant with respect to the E-mode power spectrum above $\ell = 150$.

7.2.4 Uneven intra-pixel coverage

Simulating a CMB experiment using a more realistic scanning strategy can produce another systematic effect at the power spectra level. This source of noise is related to the intra-pixel coverage of the sky. In §6.2, all pixels were observed exactly at their centers while, in a real experiment, every sample of the TOD "hits" a given pixel at an arbitrary location within it. If the distribution of hits inside a pixel is symmetric with respect to pixel center coordinates, map-making will average all observations and the power spectra from the resulting map will not be affected. However, if this distribution is asymmetric and gradients between pixels are present (recall that pixel space convolution is affected by neighbor pixels) the resulting power spectra may suffer from P to P leakage. This was discussed in more detail in more detail in the literature (see [23]) and shown to be a realistic effect in Section 6.3.

Figure 14 shows the result of running the realistic simulation with matched pointing and matched beams with the addition of a polarized CMB with $r = 0.1$. A spurious signal is present in the B-mode power spectrum, showing oscillatory behavior up $\ell = 160$ and increasing as a power-law afterwards. In the upper plot of Figure 12, the same simulation was performed but with an unpolarized CMB as input, the resulting polarized power spectra being consistent with zero. This indicates that the effect of uneven intra-pixel coverage is P to P leakage, as mention in Section 6.3. This systematic effect is subdominant with respect to the T to P leakage caused by pointing and beam mismatch at all scales, as well as having a lower amplitude than a theoretical primordial B-mode power spectrum for $r = 0.1$ up to $\ell = 200$. It is worth noting that this P to P leakage is due to an uneven convolution of the pixel window and, unlike the other effects studied here, can be mitigated as more data is added when using a well planned scanning strategy.

8 Conclusions

In this work, we have presented a method for simulating the interaction between the electromagnetic properties of an antenna and a polarized sky in the context of CMB experiments.

We have also described PISCO, a new computer simulation code that implements this method. PISCO is capable of generating beam-convolved timestreams for arbitrary beams, sky models and scanning strategies and is designed to exploit the natural parallelism in the pixel space convolution algorithm by offloading the computation to the GPU. We performed tests applying PISCO to several scenarios: point source convolution, an ideal and a more realistic CMB experiment, this last set of tests was based on the CLASS experiment. We showed that PISCO is able to reproduce the expected effects that pointing mismatch, beam mismatch and uneven intra-pixel coverage have on CMB power spectra.

We are not aware of any other publicly available code that performs pixel space convolution using a formalism that is similar to one used by PISCO, the only documented code that performs pixel space convolution being FEBeCop. We believe PISCO will become a valuable tool when modeling the effect of noise sources that are difficult to include in harmonic space implementations like the one described in [8]. These sources include, but are not limited to, atmospheric turbulence, transient events on the sky and time-dependent behavior of the optics. It is also worth noting that PISCO can naturally include modulation techniques, like half-wave plates, when provided with a modulated model of the beamsor. Finally, the parallelism of the pixel space convolution algorithm provides an opportunity for improvement over the current implementation by harvesting the computational power of modern HPC facilities, particularly those including multiple GPU nodes.

Acknowledgments

References

[1] Prézeau, G. and Reinecke, M. Algorithm for the Evaluation of Reduced Wigner Matrices. Prezeau G., Reinecke M., 2010, ApJS, 190, 267. DOI 10.1088/0067-0049/190/2/267.

[2] John W. Appel, Zhilei Xu, Ivan L. Padilla, Kathleen Harrington, Bastián Pradenas Marquez, Aamir Ali, Charles L. Bennett, Michael K. Brewer, Ricardo Bustos, Manwei Chan, David T. Chuss, Joseph Cleary, Jullianna Couto, Sumit Dahal, Kevin Denis, Rolando Dünner, Joseph R. Eimer, Thomas Essinger-Hileman, Pedro Fluxa, Dominik Gothe, Gene C. Hilton, Johannes Hubmayr, Jeffrey Iuliano, John Karakla, Tobias A. Marriage, Nathan J. Miller, Carolina Núñez, Lucas Parker, Matthew Petroff, Carl D. Reintsema, Karwan Rostem, Robert W. Stevens, Deniz Augusto Nunes Valle, Bingjie Wang, Duncan J. Watts, Edward J. Wollack, and Lingzhen Zeng. On-sky Performance of the CLASS Q-band Telescope. *APJ*, 876(2):126, May 2019.

[3] Nicholas Wilt. The CUDA handbook: a comprehensive guide to GPU programming. *Addison-Wesley*, 2019.

[4] BICEP2 Collaboration, Keck Array Collaboration, P. A. R. Ade, Z. Ahmed, R. W. Aikin, K. D. Alexand er, D. Barkats, S. J. Benton, C. A. Bischoff, J. J. Bock, R. Bowens-Rubin, J. A. Brevik, I. Buder, E. Bullock, V. Buza, J. Connors, J. Cornelison, B. P. Crill, M. Crumrine, M. Dierickx, L. Duband, C. Dvorkin, J. P. Filippini, S. Fliescher, J. Grayson, G. Hall, M. Halpern, S. Harrison, S. R. Hildebrand t, G. C. Hilton, H. Hui, K. D. Irwin, J. Kang, K. S. Karkare, E. Karpel, J. P. Kaufman, B. G. Keating, S. Kefeli, S. A. Kernasovskiy, J. M. Kovac, C. L. Kuo, N. A. Larsen, K. Lau, E. M. Leitch, M. Lueker, K. G. Megerian, L. Moncelsi, T. Namikawa, C. B. Netterfield, H. T. Nguyen, R. O'Brient, R. W. Ogburn, S. Palladino, C. Pryke, B. Racine, S. Richter, A. Schillaci, R. Schwarz, C. D. Sheehy, A. Soliman, T. St. Germaine, Z. K. Staniszewski, B. Steinbach, R. V. Sudiwala, G. P. Teply, K. L. Thompson, J. E. Tolan, C. Tucker, A. D. Turner, C. Umiltà, A. G. Vieregg, A. Wand ui, A. C. Weber, D. V. Wiebe, J. Willmert, C. L. Wong, W. L. K. Wu, H. Yang, K. W. Yoon, and C. Zhang. Constraints on Primordial Gravitational

Waves Using Planck, WMAP, and New BICEP2/Keck Observations through the 2015 Season. *PRL*, 121:221301, Nov 2018.

[5] Anthony Challinor, Pablo Fosalba, Daniel Mortlock, Mark Ashdown, Benjamin Wandelt, and Krzysztof Górski. All-sky convolution for polarimetry experiments. *PRD*, 62:123002, Dec 2000.

[6] G. Chon, A. Challinor, S. Prunet, E. Hivon, and I. Szapudi. Fast estimation of polarization power spectra using correlation functions. *MNRAS*, 350:914–926, May 2004.

[7] Santanu Das, Sanjit Mitra, and Sonu Tabitha Paulson. Effect of noncircularity of experimental beam on CMB parameter estimation. *Journal of Cosmology and Astro-Particle Physics*, 2015:048, March 2015.

[8] Adriaan J. Duivenvoorden, Jon E. Gudmundsson, and Alexandra S. Rahlin. Full-sky beam convolution for cosmic microwave background applications. *arXiv e-prints*, page arXiv:1809.05034, September 2018.

[9] Thomas Essinger-Hileman, Aamir Ali, Mandana Amiri, John W. Appel, Derek Araujo, Charles L. Bennett, Fletcher Boone, Manwei Chan, Hsiao-Mei Cho, David T. Chuss, Felipe Colazo, Erik Crowe, Kevin Denis, Rolando Dünner, Joseph Eimer, Dominik Gothe, Mark Halpern, Kathleen Harrington, Gene C. Hilton, Gary F. Hinshaw, Caroline Huang, Kent Irwin, Glenn Jones, John Karakla, Alan J. Kogut, David Larson, Michele Limon, Lindsay Lowry, Tobias Marriage, Nicholas Mehrle, Amber D. Miller, Nathan Miller, Samuel H. Moseley, Giles Novak, Carl Reintsema, Karwan Rostem, Thomas Stevenson, Deborah Towner, Kongpop U-Yen, Emily Wagner, Duncan Watts, Edward J. Wollack, Zhilei Xu, and Lingzhen Zeng. CLASS: the cosmology large angular scale surveyor. volume 9153 of *Society of Photo-Optical Instrumentation Engineers (SPIE) Conference Series*, page 91531I, Jul 2014.

[10] K. M. Górski, E. Hivon, A. J. Banday, B. D. Wandelt, F. K. Hansen, M. Reinecke, and M. Bartelmann. HEALPix: A Framework for High-Resolution Discretization and Fast Analysis of Data Distributed on the Sphere. *APJ*, 622:759–771, April 2005.

[11] K. M. Górski, B. D. Wandelt, E. Hivon, F. K. Hansen, and A. J. Banday. The HEALPix Primer Version 3.50, December 10, 2018, HEALPix Documentation. Accessed on: Aug. 14, 2019. [Online]. Available:https://healpix.sourceforge.io/documentation.php

[12] K. Harrington, T. Marriage, A. Ali, J. W. Appel, C. L. Bennett, F. Boone, M. Brewer, M. Chan, D. T. Chuss, F. Colazo, S. Dahal, K. Denis, R. Dünner, J. Eimer, T. Essinger-Hileman, P. Fluxa, M. Halpern, G. Hilton, G. F. Hinshaw, J. Hubmayr, J. Iuliano, J. Karakla, J. McMahon, N. T. Miller, S. H. Moseley, G. Palma, L. Parker, M. Petroff, B. Pradenas, K. Rostem, M. Sagliocca, D. Valle, D. Watts, E. Wollack, Z. Xu, and L. Zeng. The Cosmology Large Angular Scale Surveyor. In *Millimeter, Submillimeter, and Far-Infrared Detectors and Instrumentation for Astronomy VIII*, volume 9914 of *SPIE*, page 99141K, July 2016.

[13] W. C. Jones, T. E. Montroy, B. P. Crill, C. R. Contaldi, T. S. Kisner, A. E. Lange, C. J. MacTavish, C. B. Netterfield, and J. E. Ruhl. Instrumental and analytic methods for bolometric polarimetry. *AAP*, 470:771–785, August 2007.

[14] Antony Lewis and Sarah Bridle. Cosmological parameters from CMB and other data: A Monte Carlo approach. *PRD*, 66:103511, 2002.

[15] A. Ludwig. The definition of cross polarization. *IEEE Transactions on Antennas and Propagation*, 21(1):116–119, January 1973.

[16] N. J. Miller, D. T. Chuss, T. A. Marriage, E. J. Wollack, J. W. Appel, C. L. Bennett, J. Eimer, T. Essinger-Hileman, D. J. Fixsen, K. Harrington, S. H. Moseley, K. Rostem, E. R. Switzer, and D. J. Watts. Recovery of Large Angular Scale CMB Polarization for Instruments Employing Variable-delay Polarization Modulators. *APJ*, 818(2):151, Feb 2016.

[17] S. Mitra, G. Rocha, K. M. Górski, K. M. Huffenberger, H. K. Eriksen, M. A. J. Ashdown, and C. R. Lawrence. Fast Pixel Space Convolution for Cosmic Microwave Background Surveys with Asymmetric Beams and Complex Scan Strategies: FEBeCoP. *The Astrophysical Journal Supplement Series*, 193:5, March 2011.

[18] D. O'Dea, A. Challinor, and B. R. Johnson. Systematic errors in cosmic microwave background polarization measurements. *MNRAS*, 376:1767–1783, April 2007.

[19] L. Page, C. Barnes, G. Hinshaw, D. N. Spergel, J. L. Weiland, E. Wollack, C. L. Bennett, M. Halpern, N. Jarosik, A. Kogut, M. Limon, S. S. Meyer, G. S. Tucker, and E. L. Wright. First-Year Wilkinson Microwave Anisotropy Probe (WMAP) Observations: Beam Profiles and Window Functions. *The Astrophysical Journal Supplement Series*, 148:39–50, September 2003.

[20] Jeffrey R. Piepmeier, David G. Long, and Eni G. Njoku. Stokes antenna temperatures. *IEEE Transactions on Geoscience and Remote Sensing*, 46(2):516–527, 2008.

[21] Planck Collaboration, P. A. R. Ade, N. Aghanim, M. Arnaud, M. Ashdown, J. Aumont, C. Baccigalupi, A. J. Banday, R. B. Barreiro, J. G. Bartlett, N. Bartolo, E. Battaner, K. Benabed, A. Benoît, A. Benoit-Lévy, J. P. Bernard, M. Bersanelli, P. Bielewicz, J. J. Bock, A. Bonaldi, L. Bonavera, J. R. Bond, J. Borrill, F. R. Bouchet, F. Boulanger, M. Bucher, C. Burigana, R. C. Butler, E. Calabrese, J. F. Cardoso, G. Castex, A. Catalano, A. Challinor, A. Chamballu, H. C. Chiang, P. R. Christensen, D. L. Clements, S. Colombi, L. P. L. Colombo, C. Combet, F. Couchot, A. Coulais, B. P. Crill, A. Curto, F. Cuttaia, L. Danese, R. D. Davies, R. J. Davis, P. de Bernardis, A. de Rosa, G. de Zotti, J. Delabrouille, J. M. Delouis, F. X. Désert, C. Dickinson, J. M. Diego, K. Dolag, H. Dole, S. Donzelli, O. Doré, M. Douspis, A. Ducout, X. Dupac, G. Efstathiou, F. Elsner, T. A. Enßlin, H. K. Eriksen, J. Fergusson, F. Finelli, O. Forni, M. Frailis, A. A. Fraisse, E. Franceschi, A. Frejsel, S. Galeotta, S. Galli, K. Ganga, T. Ghosh, M. Giard, Y. Giraud-Héraud, E. Gjerløw, J. González-Nuevo, K. M. Górski, S. Gratton, A. Gregorio, A. Gruppuso, J. E. Gudmundsson, F. K. Hansen, D. Hanson, D. L. Harrison, S. Henrot-Versillé, C. Hernández-Monteagudo, D. Herranz, S. R. Hildebrandt, E. Hivon, M. Hobson, W. A. Holmes, A. Hornstrup, W. Hovest, K. M. Huffenberger, G. Hurier, A. H. Jaffe, T. R. Jaffe, W. C. Jones, M. Juvela, A. Karakci, E. Keihänen, R. Keskitalo, K. Kiiveri, T. S. Kisner, R. Kneissl, J. Knoche, M. Kunz, H. Kurki-Suonio, G. Lagache, J. M. Lamarre, A. Lasenby, M. Lattanzi, C. R. Lawrence, R. Leonardi, J. Lesgourgues, F. Levrier, M. Liguori, P. B. Lilje, M. Linden-Vørnle, V. Lindholm, M. López-Caniego, P. M. Lubin, J. F. Macías-Pérez, G. Maggio, D. Maino, N. Mand olesi, A. Mangilli, M. Maris, P. G. Martin, E. Martínez-González, S. Masi, S. Matarrese, P. McGehee, P. R. Meinhold, A. Melchiorri, J. B. Melin, L. Mendes, A. Mennella, M. Migliaccio, S. Mitra, M. A. Miville-Deschênes, A. Moneti, L. Montier, G. Morgante, D. Mortlock, A. Moss, D. Munshi, J. A. Murphy, P. Naselsky, F. Nati, P. Natoli, C. B. Netterfield, H. U. Nørgaard-Nielsen, F. Noviello, D. Novikov, I. Novikov, C. A. Oxborrow, F. Paci, L. Pagano, F. Pajot, D. Paoletti, F. Pasian, G. Patanchon, T. J. Pearson, O. Perdereau, L. Perotto, F. Perrotta, V. Pettorino, F. Piacentini, M. Piat, E. Pierpaoli, D. Pietrobon, S. Plaszczynski, E. Pointecouteau, G. Polenta, G. W. Pratt, G. Prézeau, S. Prunet, J. L. Puget, J. P. Rachen, R. Rebolo, M. Reinecke, M. Remazeilles, C. Renault, A. Renzi, I. Ristorcelli, G. Rocha, M. Roman, C. Rosset, M. Rossetti, G. Roudier, J. A. Rubiño-Martín, B. Rusholme, M. Sandri, D. Santos, M. Savelainen, D. Scott, M. D. Seiffert, E. P. S. Shellard, L. D. Spencer, V. Stolyarov, R. Stompor, R. Sudiwala, D. Sutton, A. S. Suur-Uski, J. F. Sygnet, J. A. Tauber, L. Terenzi, L. Toffolatti, M. Tomasi, M. Tristram, M. Tucci, J. Tuovinen, L. Valenziano, J. Valiviita, B. Van Tent, P. Vielva, F. Villa, L. A. Wade, B. D. Wandelt, I. K. Wehus, N. Welikala, D. Yvon, A. Zacchei, and A. Zonca. Planck 2015 results. XII. Full focal plane simulations. *AAP*, 594:A12, Sep 2016.

[22] Planck Collaboration, P. A. R. Ade, N. Aghanim, M. Arnaud, M. Ashdown, J. Aumont, C. Baccigalupi, A. J. Banday, R. B. Barreiro, J. G. Bartlett, and et al. Planck 2015 results. XIII. Cosmological parameters. *AAP*, 594:A13, September 2016.

[23] T Poutanen, Giancarlo de Gasperis, Eric Hivon, H Kurki-Suonio, Amedeo Balbi, J Borrill, C Cantalupo, Olivier Doré, E Keihanen, C R Lawrence, Davide Maino, P Natoli, S Prunet, Radek Stompor, and Romain Teyssier. Comparison of map-making algorithms for cmb experiments. *Astronomy and Astrophysics*, 01 2005.

[24] Jason Sanders and Edward Kandrot. *CUDA by example: an introduction to general-purpose GPU programming.* Addison-Wesley Professional, 2010.

[25] Meir Shimon, Brian Keating, Nicolas Ponthieu, and Eric Hivon. Cmb polarization systematics due to beam asymmetry: Impact on inflationary science. *Phys. Rev. D*, 77:083003, Apr 2008.

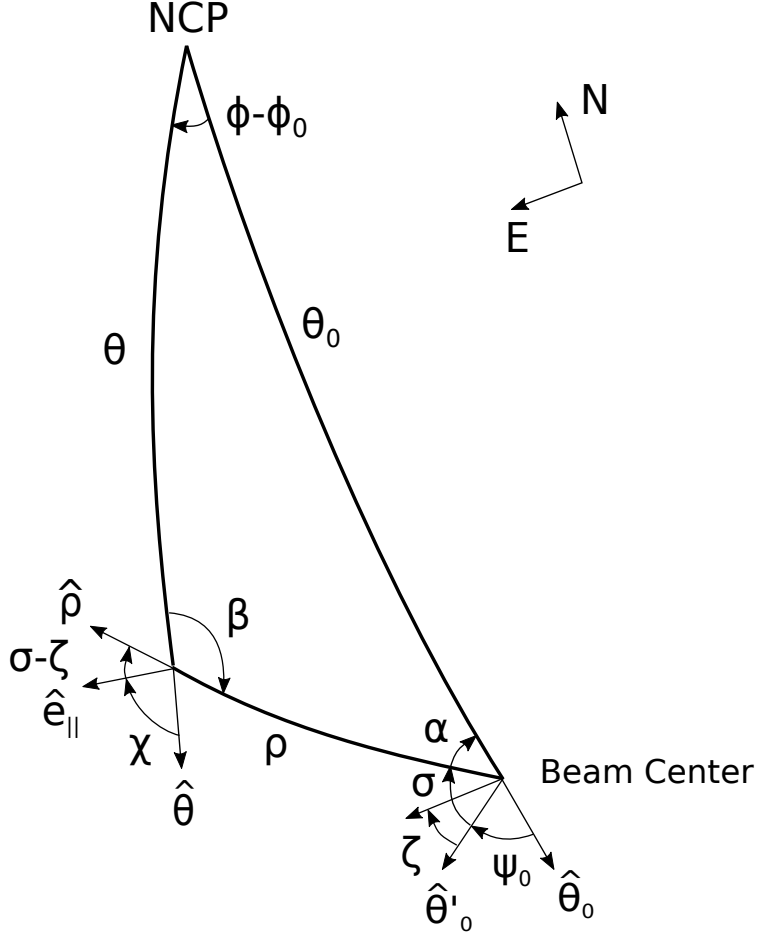[26] Benjamin D. Wandelt and Krzysztof M. Górski. Fast convolution on the sphere. *PRD*, 63:123002, Jun 2001.

Figure 15. Sky and antenna basis coordinates for beam center pointing and off beam center pointing from the viewpoint of an observer looking at the sky. Here NCP is the North Celestial Pole and χ is the angle between $\hat{e}_{\parallel}$ and $\hat{\theta}$ according to Ludwig's 3rd definition.

A Computation of antenna basis coordinates and the co-polarization angle from sky coordinates

For a beam center pointing (θ_0, ϕ_0), rotation angle ψ_0 and off beam center pointing (θ, ϕ) in the sky basis, we can derive the antenna basis coordinates (ρ, σ) and the angle χ between $\hat{e}_{\parallel}$ and $+Q$ ($\hat{\theta}$) by using spherical trigonometry (see Figure 15). The identities used in this derivation are: the law of cosines, the law of sines and the analogue (or five part) formula.

Defining $\Delta\phi \equiv \phi - \phi_0$, the antenna basis coordinate ρ is given by

$$\rho = \arccos(\cos(\theta)\cos(\theta_0) + \sin(\theta)\sin(\theta_0)\cos(\Delta\phi)). \tag{A.1}$$

Then, defining α as the angle between ρ and θ_0, the antenna basis coordinate σ is given by

$$\sin(\alpha) = \frac{\sin(\theta)\sin(\Delta\phi)}{\sin(\rho)} \tag{A.2}$$

$$\cos(\alpha) = \frac{\cos(\theta)\sin(\theta_0) - \sin(\theta)\cos(\theta_0)\cos(\Delta\phi)}{\sin(\rho)} \tag{A.3}$$

$$\alpha = \arctan\left(\frac{\sin(\theta)\sin(\Delta\phi)}{\cos(\theta)\sin(\theta_0) - \sin(\theta)\cos(\theta_0)\cos(\Delta\phi)}\right) \tag{A.4}$$

$$\sigma = 180° - \psi_0 - \alpha. \tag{A.5}$$

Following Ludwig's third definition of cross polarization, substituting $\sigma + 90°$ for Ludwig's ϕ (see [15]), the unit vectors of co and cross polarization for a detector aligned at an angle ζ with respect to the basis vector $\hat{\theta}_0'$ in the antenna basis are

$$\hat{e}_\| = \cos(\sigma - \zeta)\hat{\rho} - \sin(\sigma - \zeta)\hat{\sigma} \tag{A.6}$$

$$\hat{e}_\times = -\sin(\sigma - \zeta)\hat{\rho} - \cos(\sigma - \zeta)\hat{\sigma}. \tag{A.7}$$

Thus $\hat{e}_\|$ is offset from $\hat{\rho}$ by the angle $\zeta - \sigma$. Then, defining β as the angle between θ and ρ, yields

$$\sin(\beta) = \frac{\sin(\theta_0)\sin(\Delta\phi)}{\sin(\rho)} \tag{A.8}$$

$$\cos(\beta) = \frac{\cos(\theta_0)\sin(\theta) - \sin(\theta_0)\cos(\theta)\cos(\Delta\phi)}{\sin(\rho)} \tag{A.9}$$

$$\beta = \arctan\left(\frac{\sin(\theta_0)\sin(\Delta\phi)}{\cos(\theta_0)\sin(\theta) - \sin(\theta_0)\cos(\theta)\cos(\Delta\phi)}\right) \tag{A.10}$$

$$\chi = \beta + \zeta - \sigma. \tag{A.11}$$